Physics in Medicine & Biology

IPEM Institute of Physics and Engineering in Medicine

PAPER • OPEN ACCESS

A data analysis framework for *in vivo* monitoring in carbon-ion radiotherapy (CIRT): towards 3D reconstruction of interfractional anatomical changes

To cite this article: Patrice Schlegel *et al* 2025 *Phys. Med. Biol.* **70** 245009

IOP Publishing Phys. Med. Biol. 70 (2025) 245009 https://doi.org/10.1088/1361-6560/ae22bb

Physics in Medicine & Biology

IPEM Institute of Physics and Engineering in Medicine

OPEN ACCESS

RECEIVED
5 July 2025

REVISED
12 November 2025

ACCEPTED FOR PUBLICATION
21 November 2025

PUBLISHED
11 December 2025

PAPER

A data analysis framework for *in vivo* monitoring in carbon-ion radiotherapy (CIRT): towards 3D reconstruction of interfractional anatomical changes

Patrice Schlegel[1,2,3,*], **Rebekka Kirchgaessner**[1,4,6], **Pamela Ochoa Parra**[1,4,6], **Laurent Kelleter**[1,6,8], **Michael Gertz**[3], **Ralf Mikut**[5], **Oliver Jäkel**[1,2,6,7,8] and **Maria Martišíková**[1,6,8]

[1] Division of Medical Physics in Radiation Oncology, German Cancer Research Center (DKFZ), Heidelberg, Germany
[2] Medical Faculty, Heidelberg University, Heidelberg, Germany
[3] Institute of Computer Science, Heidelberg University, Heidelberg, Germany
[4] Department of Physics and Astronomy, Heidelberg University, Heidelberg, Germany
[5] Institute for Automation and Applied Informatics (IAI), Karlsruhe Institute of Technology (KIT), Karlsruhe, Germany
[6] Heidelberg Institute for Radiation Oncology (HIRO) and National Center for Radiation Research in Oncology (NCRO), Heidelberg, Germany
[7] Department of Radiation Oncology Heidelberg University Hospital, Heidelberg Ion-Beam Therapy Center (HIT), Heidelberg, Germany
[8] National Center of Tumor Diseases (NCT) Heidelberg, a partnership between DKFZ and University Medical Center Heidelberg, Heidelberg, Germany
[*] Author to whom any correspondence should be addressed.

E-mail: Patrice.Schlegel@dkfz-heidelberg.de

Keywords: carbon-ion radiation therapy, particle therapy, novel imaging methods, medical physics

Abstract

Objectives. Carbon-ion radiotherapy is a cancer treatment modality with exceptional precision and effectiveness compared to conventional x-ray therapy. Our goal is to support maintaining its precise dose administration throughout a multi-fractional radiation treatment by detecting possible anatomical changes decremental to conformal dose deposition without the need for additional imaging. To that end our work group has developed a custom detection system using TimePix3 trackers during treatment to detect the naturally occurring secondary charged particles, which carry information about the irradiated region. This enables treatment-day accurate *in-vivo* monitoring of patient anatomy without requiring additional imaging. Our goal is to provide a robust and extensible methodological framework that allows us to extract relevant information supporting clinical decision making. *Approach.* Comparing the measurements of different states of the same patient, we aim to determine if an anatomical change is present and at what location it occurred. Departing from solely utilizing statistical differences in local particle counts, the presented method exploits the spectral domain of the measurement differences. We perform a localized spectral analysis and exploit joint localized frequency band variations to robustly identify the location of changes between two measurement states. *Main Results.* We show the validity of our approach, reporting the performance results of applying our method to measurements acquired during irradiation experiments using polymethyl methacrylate head phantoms carried out at the *Heidelberg Ion Beam Therapy Center*. Furthermore, we demonstrate the flexibility of our analysis framework by showing the impact of applying filters or using alternative sub-modules in its multi-stage processing pipeline. *Significance.* We provide a data-analytical framework as well as basic analytical methods required to extract evidence for the presence of anatomical changes from secondary charged particle measurements for subsequent clinical assessment. These represent essential building blocks required to perform full 3D reconstruction of anatomical changes based solely on secondary particles.

1. Introduction

Carbon-ion radiotherapy (CIRT) (Amaldi and Kraft 2005, Tinganelli and Durante 2020) is a highly effective and precise tumor treatment option with a multitude of desirable advantages (Mizoe *et al* 2012, Mohamad *et al* 2018, Malouff *et al* 2019, Musha *et al* 2022) that make it an invaluable tool in radiation oncology. Due to the finite range of the carbon ions in tissue, with the dose maximum at the end of their range and only small lateral scattering, the dose distribution can be shaped more precisely to the tumor region than in conventional radiotherapy. Additionally, carbon ions exhibit an increased biological effectiveness as compared to protons and x-rays (Durante and Debus 2018). These advantages allow treatment closer to critical anatomical structures and thereby extends radiation treatment to cases that would not have been considered for treatment before. In general, its precision allows sparing healthy tissue from being irradiated, since the dose distribution can be shaped more precisely to the target volume.

These advantages however, come at the cost of an increased sensitivity to changes of the internal tissue structure of the patient, as well as patient positioning. The former can be caused by the treatment itself e.g. when the targeted tumor changes in volume or when swelling occurs within the treated region, or as the result of a patient's weight gain or loss. Even seasonal infections can lead to geometric changes relevant for the dose deposition, e.g. when cavities in the head and neck region fill with fluids. The consequence of such changes throughout a multi-fractional treatment is the risk of delivering the radiation dose at unintended locations. The reason is that the dose distribution depends on the (possibly changing) structure and density of the varying tissue types the beam traverses. Standard procedures followed in CIRT vary among treatment facilities and are derived from balancing medical necessity and practical feasibility and they do not generally include imaging for the purpose of anatomical change monitoring. As a consequence, not all patients are prescribed a weekly follow-up CT, as imaging is decided at the physicians' discretion. Ideally, physicians would obtain sufficient and individual (patient and time dependent) reason to trigger additional imaging.

Our goal, therefore, is to provide sufficient evidence for or against the presence of relevant anatomical changes, in order to either justify the resource-intensive, time-consuming, and radiation-bearing process of additional imaging or avoid it. To that end we seek to develop *in-vivo* monitoring by means of measurements of secondary charged particle emissions, a naturally occurring by-product of the irradiation process. These secondary charged particles are produced by nuclear interactions of the primary carbon ions (projectile) with target nuclei which can lead to the fragmentation both of the projectile and the target. Projectile fragments can thereby receive sufficient kinetic energy to escape the patient (Gunzert-Marx *et al* 2008). The general approach developed in our work group is to detect and exploit the paths of these charged nuclear fragments. Their distribution carries information about the structure of the matter it traversed (Henriquet *et al* 2012, Schweins *et al* 2025). This non-invasive monitoring approach does not interfere with the treatment process and can be integrated into the clinical workflow more seamlessly than comparable in-vivo monitoring methods (Parodi and Polf 2018). Obtaining secondary ion-track information in a clinical setting is made possible by employing the custom multi-tracker system developed by our group (Kelleter *et al* 2024a). In our group's initial successful feasibility study (Ghesquière-Diérickx *et al* 2021), we investigated the influence of the detection angles and showed that at angles around 30° the best compromise between detectability and localization accuracy in the spatial domain was observed and changes could be detected with high statistical significance.

Prior work on utilizing the secondary charged particle measurements for change detection were focused on determining the locations of statistically relevant differences between the two analyzed measurement sets. This meant that locations where the number of particles differed to a statistically sufficient degree were assumed to indicate anatomical changes (Gwosch *et al* 2013, Gaa *et al* 2017, Reinhart *et al* 2017), an approach we consider the baseline for comparing our method's performance. The small difference in particle amounts makes detection in this way challenging and very sensitive to the actual number of secondary charged particles measured at individual locations. Furthermore, the detected particle amounts depend on a combination of factors with varying contributions between treatment fractions, including clinical (tumor depth and position, prescribed fraction dose), particle-physical (multiple scattering and energy loss of fragments), and detector setup-related (detector positioning, solid angle acceptance, and resolution) (Muraro *et al* 2016).

A more robust, flexible and extensible set of methods is therefore desirable when aiming for clinical applications. To this end we need to (a) investigate and describe the structure of the measurement data as well as (b) determine the limitations of what type and magnitude of changes can be detected and localized by analyzing solely the measurement data and (c) identify and develop the basic data analytical building blocks and extend their capabilities in systematic increments. The results presented in this

manuscript are aimed at contributing to all above mentioned points while using measurements acquired during precisely controlled experimental setups with polymethyl methacrylate (PMMA) head phantoms.

The focus of this manuscript is to present a method for detecting and localizing the changes between two sets of secondary charged particle measurements along the beam direction. The chosen setup is close to the practical clinical scenario, where the measurements of two treatment fractions of the same patient are analyzed to determine whether there are detectable anatomical changes between them. The experiments were performed with a cylindrical head-sized homogeneous PMMA phantom with exchangeable air-filled cavities irradiated with a realistic CIRT treatment plan. We determine the achieved depth-detection accuracy over a set of well-defined experiments and analyze the method's robustness to clinically relevant uncertainties. We provide essential computational procedure to be used as building blocks for a future full 3D reconstruction.

2. Materials and methods

2.1. Data acquisition

2.1.1. Experimental setups

The experimental data used to validate our approach were collected at the *Heidelberg Ion Beam Therapy Center (HIT)* facility throughout irradiation experiments conducted during the rigorous test and validation phase of our group's detection system. We therefore have the advantage of being able to utilize data that was specifically designed to assess the suitability of any analysis approach to be applied to measurements of the now ongoing clinical study involving patients with tumors in the head and neck region. The clinical changes between the fractions of a series of treatments are expected to be small and the experimental setup therefore gradually approaches smaller changes represented by air cavities of decreasing volume.

Experimental conditions are kept as close to the clinical reality as possible using the actual treatment facility and the exact beam parameters used for patients with a clinically realistic treatment plan designed for a spherical tumor of $\approx 50\,\text{mm}$ diameter located at the isocenter. The head in these experimental setups is represented by a PMMA cylinder (see figure 1) with a diameter of 160 mm and a height of 90 mm with slots that allow differently sized air cavities to be created. The head phantom was placed with its center aligned with the isocenter of the treatment room (as well as the irradiated region) and the cavities were placed perpendicular to the treatment beam axis. The paths of secondary charged particles were then measured using a *mini tracker unit* based on a *Timepix3* detector. It was placed at an angle of 30° with respect to the treatment axis outside the head phantom as depicted in figure 1(a) and (b). The detection angle of 30° was chosen as based on the results of an involved experimental procedure conducted in our work group (Ghesquière-Diérickx *et al* 2021, 2022), identifying the best compromise between detectability and depth localization. The detector was positioned at a distance of 12.0 cm from the isocenter during the experiments with large cavities and at 20.7 cm at the small cavity measurements. Taking into account practical limitations including where a measurement device can be placed in a clinical setting (Kelleter *et al* 2024a) and the maximum data rate of the detector readout system (Tureček *et al* 2016).

Two sets of experimental setups were used in this work. The first consists of measurements of large (slab-shaped) air cavities of $70\,\text{mm} \times 70\,\text{mm}$ (transverse plane) with 2 mm thickness which were placed at four different depths of $-40\,\text{mm}, -22\,\text{mm}, 0\,\text{mm}$, and $+18\,\text{mm}$ along the beam axis (with respect to the isocenter) (Ghesquière-Diérickx *et al* 2021). The cavities cover the entire irradiated region as shown in figure 1(d) on the right, with the consequence that all treatment particles will have to pass through it, yielding the maximum amount of interaction with the change of material density present in its way. The second set consists of measurements of coin-shaped cavities of 20 mm diameter (transverse plane) and a thickness of 4 mm placed at $-40\,\text{mm}, -30\,\text{mm}, -20\,\text{mm}, -10\,\text{mm}, 0\,\text{mm}$ and $+10\,\text{mm}$ (Félix-Bautista *et al* 2021), they cover only a fraction of the treatment beam see figure 1(c). Their volume however is comparable to that of a change caused by blockages in clinical targets and therefore closer to the type of changes expected in a real clinical setting.

For the experiments conducted in this work, a virtual spherical tumor of $\approx 50\,\text{mm}$ was positioned at the center of the phantom, placed at the isocenter and a typical treatment of 60 Gy(RBE) in 20 fractions was prescribed. This results in a fraction dose of 3 Gy(RBE), which was delivered using the raster scanning technique with energies between 167 and 246 MeV n^{-1}. In the case of the experiments with large (slab-shaped) cavities the treatment plan covered a *planning target volume (PTV)* of $70.06\,\text{cm}^3$, which was targeted with a single-field irradiation, consisting of 19 energy layers, 8356 pencil beam spots and 5.7×10^8 primary carbon ions. For the experiments with the small (coin-shaped) cavities a treatment plan covering a PTV of $49.93\,\text{cm}^3$ was used. In this case an even more realistic irradiation with two

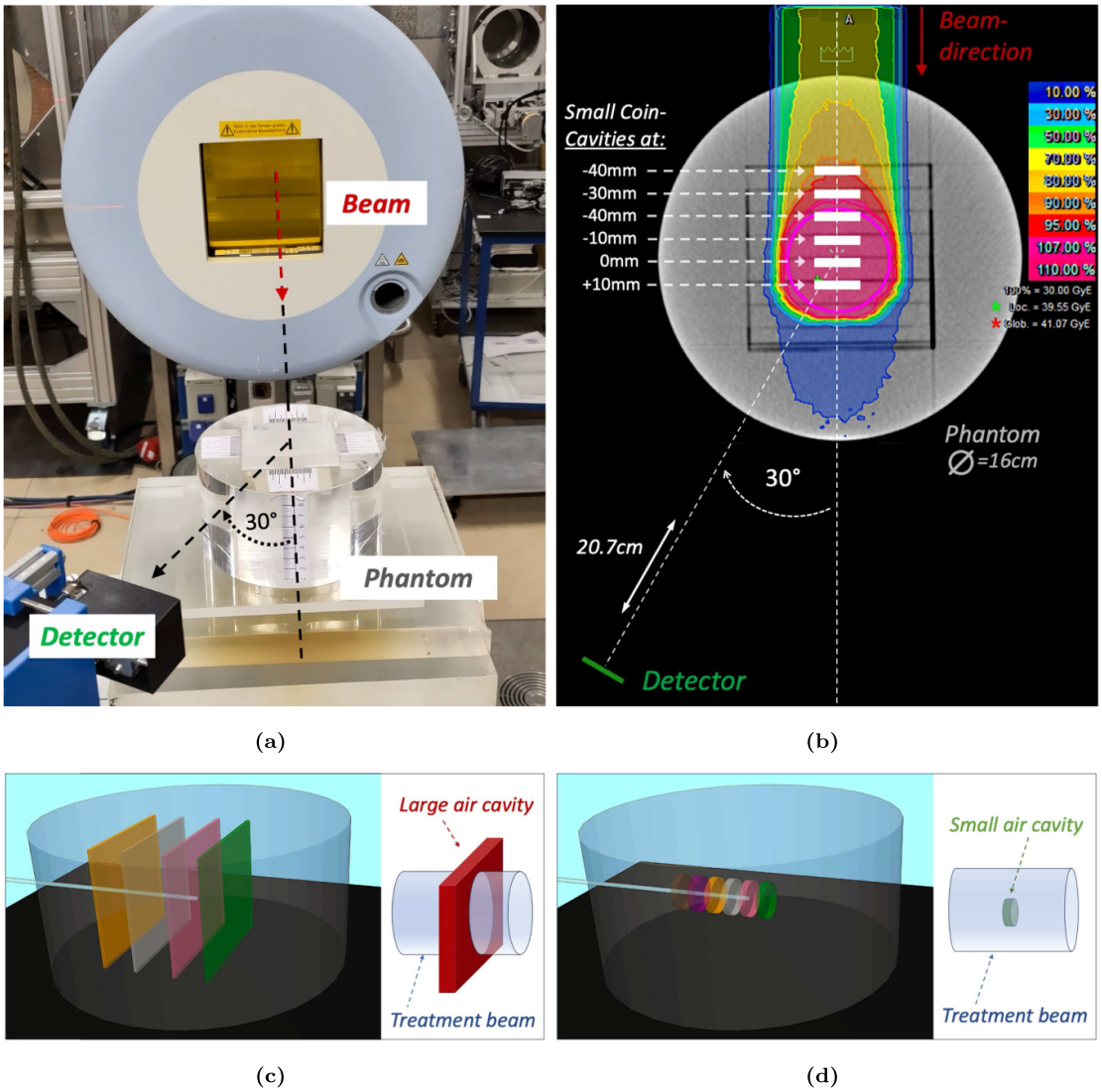

Figure 1. (a) Photograph of detection setup; (b) Top-down view with treatment plan and experimental details of the small coin-shaped cavity setups; (c) 3D rendering of experiment with head phantom, showing all large slab-shaped cavities at once; (c) (right) Visualization of the slab-shaped cavity covering the entire irradiated region. (d) (left) same as (c)(left) with all small coin-shaped cavities shown at once; (d) (right) Visualization of the irradiated region being much larger than the small air cavity.

opposing fields was chosen in the planning process, out of which one field was used for the experiments presented here. This field contained 19 energy layers, 7437 pencil beam spots and 2.5×10^8 primary carbon ions.

2.1.2. Detection system

This work utilizes measurements acquired at different phases of our group's effort to build a detection system throughout ready for clinical use. Therefore, different experimental setups designed for system and method validation were used. All measurements in this work were performed using two-layer mini-tracker detection systems based on *Timepix3* hybrid silicon pixel detectors developed by *Advacam s.r.o., Prague, Czech Republic*. These custom-built systems feature layered hybrid silicon pixel detectors with front and back detection layers, forming a telescope setup that enables charged nuclear fragment tracking and vertex reconstruction (see figure 2(a)). The measurements on the experimental setups with large cavities were carried out using a *Timepix3* module with a single 256×256pixels with a sensitive area of $\approx 1.96\,\mathrm{cm}^2$ and a silicon sensor thickness $300\,\mu$m per layer, with layer distance 2.5 cm. For the measurements of small cavities, a customized *AdvaPIX TPX3 Quad* detector module with a total surface of $3.92\,\mathrm{cm}^2$ (arranged side-by-side as 512×256 pixels) with a silicon sensor thickness $500\,\mu$m and a layer distance of 2.1 cm was used once it became available.

In both configurations, the detectors were operated in event-driven mode to optimize data throughput and ensure the registration of individual particle events. The average number of detected particles

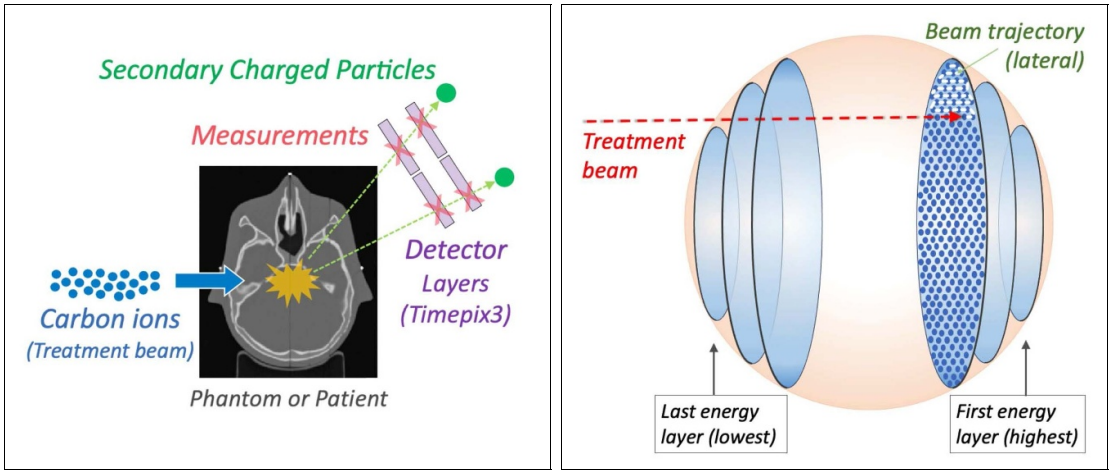

(a) (b)

Figure 2. (a) Principle of detecting secondary charged particles using a tracker setup (and an anthropomorphic head phantom). (b) Dose delivery by pencil beam scanning: a large number of individual locations are irradiated along a pre-defined trajectory at various energy levels that reach different depths.

per irradiation run was $\approx 3.03 \times 10^5$ for the large cavity setup and $\approx 1.81 \times 10^5$ for the small cavity setup. Detailed descriptions and characterizations of the devices and the detection setup used can be found in Ghesquière-Diérickx *et al* (2022), Kelleter *et al* (2024a, 2024b).

2.2. Input for data analysis

2.2.1. Data properties and attributes

The raw data consists of per-pixel data records of the *time of arrival (ToA)* timestamp of the detection event. The tracking principle is based on associating front- and back detector layer hits within a 150 ns time window and building a track by constructing a 3D vector from them. It identifies the 3D point at which the fragment path is closest (in terms of its Euclidean distance) to the pencil beam used in the same time window. In this work we use the 3D coordinates of the fragment vertex originating within the patient resulting from the estimation procedure described in Ghesquière-Diérickx *et al* (2021, 2022).

The irradiation process carried out in the form of many consecutive pencil beams (see figure 2(b)) has a strong influence on the structure of the resulting measurement data. At this point, two basic parameters that significantly influence the structure of the measured data should be mentioned: first, the positioning of the detector at an angle of 30° with respect to the beam axis in the coronal plane (top-down view); and second, the non-symmetric placement of the detectors on one side, due to practical constraints related to the irradiation process. The first parameter was found to be optimal for the detection task through rigorous experimental verification (Ghesquière-Diérickx *et al* 2021). The second has an effect on the distribution of particles along the transverse and coronal planes such that the number of measurements increases with decreasing distance to the detector position. In addition, it results in a skewing effect on the reconstruction accuracy since the particles have to traverse increasing distances through matter before reaching the detector.

Further effects are caused by geometric structures outside the irradiated treatment field which the secondary particles need to traverse before reaching the detector. Furthermore, these reproducible out-of-field effects have been observed to have a systematic influence on particle distributions and are hereby mentioned for the sake of completeness. However, these have not been fully described yet, but are under active investigation due to their relevance for the monitoring effort. The pattern followed during the dose application via pencil beam scanning process will be contained in the location distribution of the secondary particle origins and therefore result in frequency contributions within the measurements. Whether this property has adverse effects on change localizations will have to be the subject of further investigations.

2.2.2. Track building

The post-processing starts by joining detections with a maximum time difference between consecutive signals of 500 ns to clusters. The sum of all individual energy depositions of connected pixels (including diagonal pixels) in that time window make up a cluster, and its position is defined as the energy deposition weighted centroid of its pixels. Similarly, the total deposited energy of a cluster is the sum

of energy contributions by all of its pixels. The timestamp of the earliest detected pixel in the cluster is defined as the cluster's ToA. A fragment track is constructed from mapping the centroids of the front- to the back detector clusters with the most similar ToA within a 150 ns time window and extending the magnitude of the vector between them.

2.2.3. Reconstruction of fragment origins

The reconstruction of secondary fragment origins as 3D coordinates makes use of the *beam-record file*, which is produced as a quality assurance measure by the treatment system at HIT. It contains numerous precise records of the beam properties throughout the entire treatment duration, including the location on the transverse plane. The location at which a detected fragment originated is approximated using a heuristic referred to as closest-distance projection algorithm described in Ghesquière-Diérickx *et al* (2021). It identifies the 3D point at which the reconstructed fragment track (the vector originating at the back detector and passing through the front detector) passes closest (in terms of its Euclidean distance) to the pencil beam used in the same time window. The 3D coordinate chosen as the reconstructed fragment origin is located at the center of the line connecting that closest point perpendicular to the central pencil beam axis.

2.2.4. Previous approach for data analysis

The data analysis approach previously developed by our group for detecting changes along the treatment beam axis consisted of comparing the projections (depth-profile histograms) of two sets of reconstructed fragment origins projected onto the beam axis. In the case of estimating the depth location of a single cavity, the location at the minimum of the difference between the two histograms was assumed to be the location of the cavity (Ghesquière-Diérickx *et al* 2022).

2.3. New data analysis approach for change detection

2.3.1. Overview

In this section we present our method for detecting and localizing changes between two treatment delivery fractions. It is based on the fact that materials of different densities possess different stopping power (Northcliffe and Schilling 1970). A carbon-ion beam passing through materials with sufficiently different density therefore results in measurements with detectable differences in the number of generated secondary particles when comparing to a reference measurement. Air-filled regions will cause less nuclear interactions and in effect, less secondary particles to be generated than the much denser PMMA material surrounding it. Prior analysis of the measurement data compared local amounts of reconstructed secondary particle origins between two measurement sets to detect and localize changes based on statistical differences (Reinhart *et al* 2017, Kelleter *et al* 2024b). These are particularly sensitive to local variations in the detected number of particles which are a common occurrence in a measurement process based on the detection of phenomena of a stochastic nature. Our approach focuses on exploiting a before unused source of information contained in the data, namely their frequency structure. The underlying assumption is that changing distributions of particle amounts, which are the consequence of changes in the anatomy in the irradiated regions, are expected to result in discernible local variations in the frequency composition of the reconstructed particle origins. These should be especially dominant at transitions between different types of matter. The higher the density of particle origins, the more higher frequency components are contained in the signal. In the case of analyzing the difference histogram of measurements along the beam axis, this means that two different parameters contribute to the frequency composition at a specific location, (1) the difference in the number of particles at that location and (2) the variation of that difference over a local neighborhood. Therefore, especially a rapid change between two sufficiently different dense materials should be detectable as a shift in the frequency contributions.

We employ the procedure depicted in figure 3 using the data analysis methods described in the following sections along these main steps:

(i) Compute the difference histogram of the two measurements along the beam axis.
(ii) Compute the *Gabor Spectrogram* to obtain binned frequency spectra for individual locations.
(iii) Compute the correlation matrix of the binned spectra to obtain how similar frequency variations are at different locations.
(iv) Accumulate the columns of the correlation matrix to identify regions of joint variational difference to other locations.
(v) Detect the cavity location by analyzing the gradients of the accumulation function.

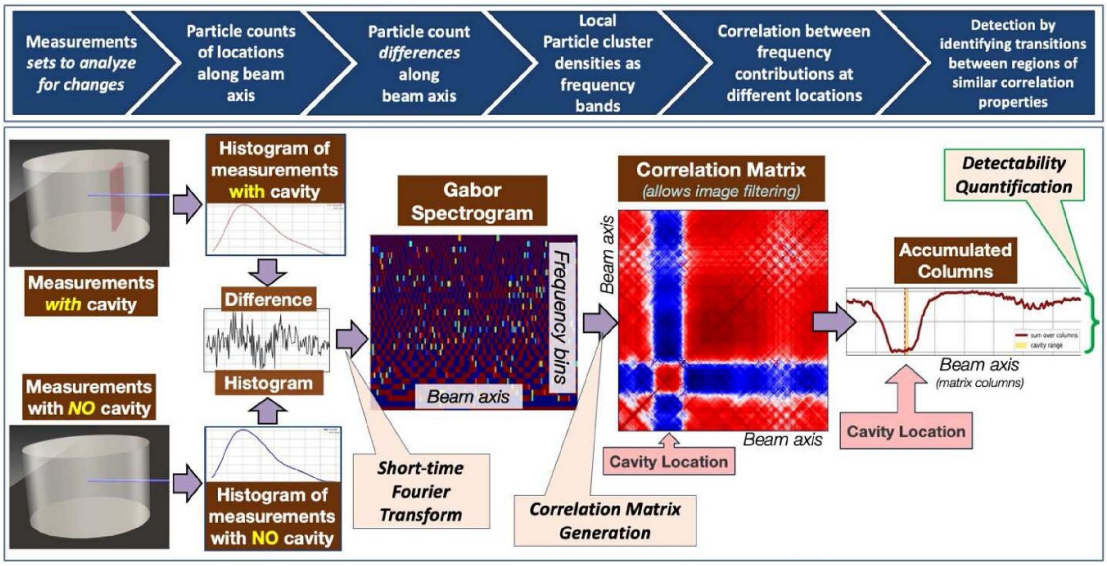

Figure 3. Process diagram of the detection method showing the sequence, computational processes and intermediate data products.

2.3.2. Fragment emission profile analysis

The initial step in the change detection procedure consists of determining the distributions of the z-coordinates (in treatment beam direction) of the reconstructed secondary charged particle origins. The histogram contains the absolute number of particles at each of N bins (location intervals) of equal size along the beam axis. We require two sets of measurements to perform the detection procedure: (1) the 'current' - containing the cavity in our experiments and (2) the 'reference' - containing no cavity. In the clinical process these would be two measurements of different treatment fractions with the reference having been acquired at the earlier stage. To perform the depth detection of an anatomical change, as it is the goal in this manuscript, we determine the difference histogram by bin-wise subtracting the 'reference' from the 'current'. Up to this point, the procedure is the same as in our group's previous data analysis (see Kelleter *et al* 2024a).

2.3.3. Analysis of fragment emission profiles in the spectral domain

The next step involves transferring the analysis into the spectral domain. This represents a major distinction to previous approaches, which estimated the cavity locations based on direct histogram comparison. By analyzing the spectral domain, it is possible to identify patterns and trends in the measurements, that may be difficult to uncover in the spatial domain. To obtain the spectral information of the difference histogram, we perform *Fourier Analysis* (Attinger *et al* 1966, Nastar and Ayache 1996, Bracewell 2012), the standard method for decomposing a signal into its frequency components. In this work we utilize the discrete Fourier transform (see equation (1)) which allows the difference histogram to be expressed in terms of a combination of orthogonal periodic basis functions. This means transforming a discrete number of equidistant samples (in the spatial domain) into complex *Fourier coefficients* $y[n]$, representing the contribution of equally distributed frequency bins. The employed transformation creates frequency bins such that the covered spectrum is provided in terms of the same number of values as the input signal, which preserves invertibility of the transform. Hence, these coefficients allow the original signal to be recovered in an inverse procedure with only minimal loss. In the case of analyzing secondary charged particle measurements the signal subjected to the *Fourier transform* is that of the difference histogram $h[n]$ between the two compared measurements of secondary charged particles along the beam axis:

$$h[n] = \sum_{i=0}^{N-1} y[i] \cdot \mathrm{e}^{-j\frac{2\pi}{N}in}, \quad n = 0, 1, \ldots, N-1 \tag{1}$$

with:

$h[n]$: Output vector of$N$ values in the frequency domain,
$y[i]$: Input sequence of N samples in the spatial domain,
i: Location index,

n: Frequency bin index (corresponds to the nth frequency component),
N: Number of location bins being transformed, (and therefore, also the number of discrete frequency bins produced),
$e^{-j\frac{2\pi}{N}in}$: Complex exponential term representing the sinusoidal basis functions,
j: Imaginary number, where $j^2 = -1$.

The output of a *Fourier transform* of a signal provides us with the composition of the frequencies contained in that signal, in our case for the entire considered span of the beam axis. This means that it will not allow us to determine which frequency composition was present at a specific location. Since in this work our goal is to pinpoint particular 'locations' along the beam axis at which a distinguishable composition of frequencies can be found we need to employ a method that is capable of providing this information, namely the *short time Fourier transform* producing a *Gabor Spectrogram* (Gabor 1946). A visualization is shown in figure 4(b) and a (left) as a schematic: a matrix where each of the M columns represents the frequency content across N frequency ranges at a specific location along the beam axis. It is computed by performing a series of Fourier transforms on a sliding window along the signal which in our case is a difference histogram along the beam axis. However, this process requires an additional filtering step since each time a small window (of length M) is cropped from the original signal, a discontinuity is introduced which leads to additional unwanted frequency contributions in the Fourier transform which are not contained in the original signal. To mitigate this effect, window functions are used to filter each of the cropped window contents prior to performing the Fourier transform. A variety of window functions are available to perform the filtering and a commonly used one, the *Hanning Window* (Blackman and Tukey 1958) defined in equation (2) is the one we used for our analysis since its frequency response yields a very low amount of undesirable additional frequency contributions:

$$w[n] = 0.5 - 0.5\cos\left(\frac{2\pi n}{N-1}\right), \quad n = 0, 1, \ldots, N-1 \tag{2}$$

with:

$w[n]$: Value of the window function at index n,
N: Total number of location bins in the window (window length),
n: Index of the current location bin, ranging from 0 to $N-1$.

Our focus was to achieve high spatial resolution while maintaining sufficient frequency resolution to preserve the key spectral features of interest. Taking into account the spatial uncertainties in the measurements as well as the expected size of the cavities, we selected a window length that provides sufficient resolution to capture the target spatial features. The window length was therefore chosen to be short enough to resolve fine spatial details, but not so short that frequency resolution became inadequate. Since the window length inherently represents a trade-off between spatial localization and frequency resolution, the chosen value reflects the targeted feature size along the beam axis, which is between 2 mm and 4 mm in thickness. With the *Hanning window* applied, this corresponds to an attenuation of more than 90% at the window edges. To ensure that these features are not under-sampled and thus aliased, the stride was set in accordance with the *Nyquist-Shannon* sampling principle (Shannon 1949), to 1 mm (half the spatial frequency of the smallest target structure), providing dense enough coverage to faithfully represent spatial variations to the highest frequencies supported by the selected window length. The values of the resulting $N \times M$ matrix represent the difference signal as N frequency bands at M locations. We use only the first half of the frequency bins, since the second half contains redundant (complex-conjugate) information.

2.3.4. Exploiting joint variational frequency information

Since the *Gabor Spectrogram* provides an extended amount of information about each location along the beam axis by providing its spectral composition, we are now able to exploit joint variational information it contains. To this end we correlate (Schober *et al* 2018) the frequency band information of all possible location combinations with each other and compute the *normalized covariance matrix* $R^{\{M\times M\}}$ shown in figure 4(c) and a (right) as a schematic.

This process takes the *Gabor Spectrogram* $S^{\{N\times M\}}$, with N frequency bins and M location bins and produces a symmetric matrix $R^{\{M\times M\}}$ of *Pearson Product-moment Correlation Coefficients* (see equation (7)). Its relationship to the concept of *covariance* can be observed in equations (3) and (4).

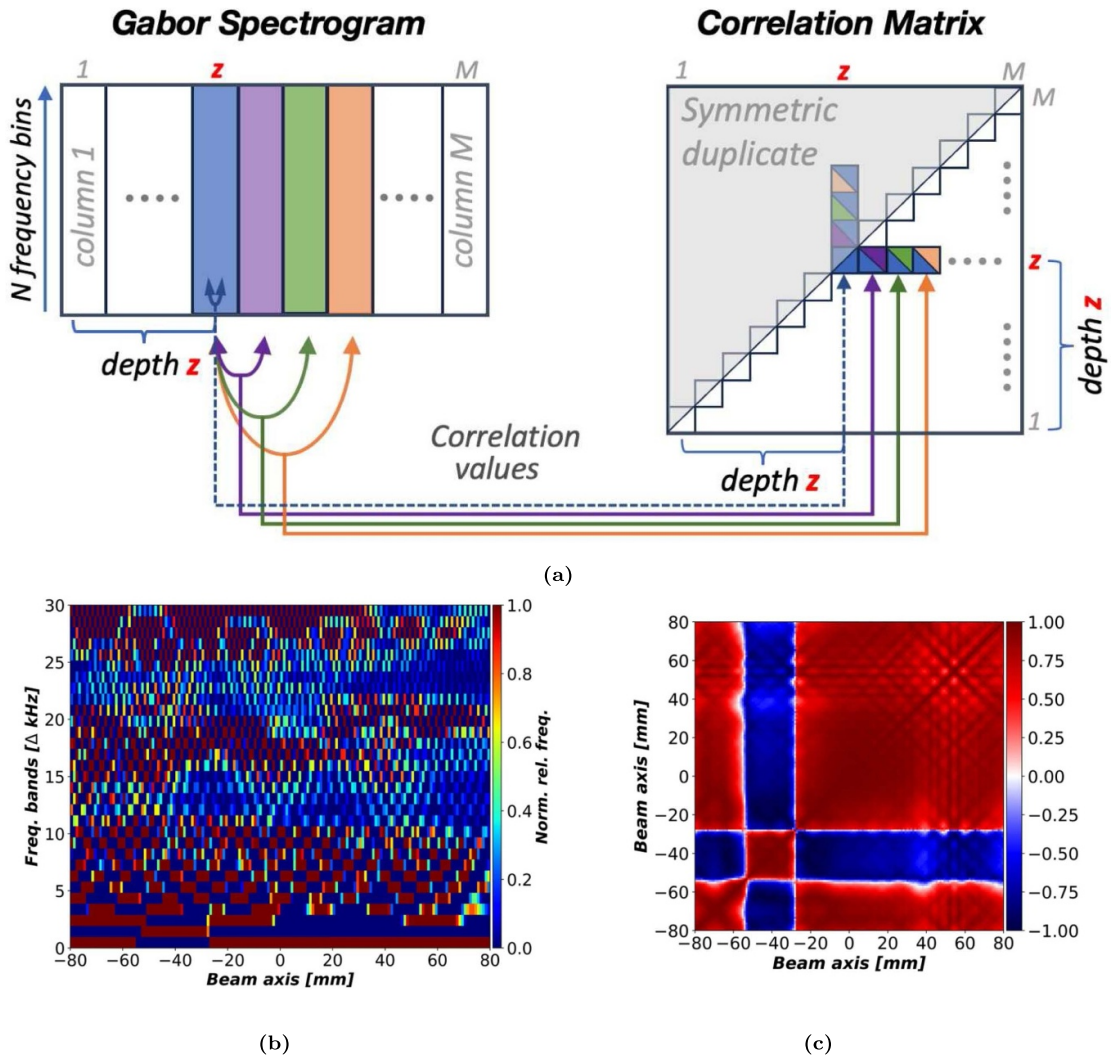

Figure 4. (a) Visualization of the correlation matrix generation process: the correlation of the two Gabor Spectrogram columns (left); results in a single correlation matrix element (indicated by the two column colors on the right); the diagonal line represents each column correlated with itself; correlating any depth location z with all other locations results in the column z, the inverse results in the row z (right). (b) Gabor Spectrogram visualization. (c) Correlation matrix visualization,

The elements $r_{i,j}$ of the correlation matrix are computed as follows:

$$r_{ij} = \frac{C_{ij}}{\sqrt{C_{ii}C_{jj}}} = \frac{\mathrm{Cov}\left(\mathbf{s}_i^\top, \mathbf{s}_j^\top\right)}{\sqrt{\mathrm{Var}\left(\mathbf{s}_i^\top\right)\ \mathrm{Var}\left(\mathbf{s}_j^\top\right)}} \tag{3}$$

with the covariance C_{ij} of columns i and j of input matrix $\mathbf{S}$:

$$C_{ij} = \mathrm{Cov}\left(\mathbf{s}_i^\top, \mathbf{s}_j^\top\right) = \frac{\sum_{k=1}^{N}\left(s_{ki} - \overline{\mathbf{s}_i^\top}\right)\left(s_{kj} - \overline{\mathbf{s}_j^\top}\right)}{N-1} \tag{4}$$

and:

$$\mathrm{Var}\left(\mathbf{s}_i^\top\right) = \frac{1}{N}\sum_{i=1}^{N}\left(\mathbf{s}_i^\top - \overline{\mathbf{s}_i^\top}\right)^2 \tag{5}$$

and the *sample mean* $\overline{\mathbf{s}_i^\top}$ of the ith column in $\mathbf{S}$:

$$\overline{\mathbf{s}_i^\top} = \frac{1}{N}\sum_{k=1}^{N} s_{ki} \tag{6}$$

such that:

$$r_{ij} = \frac{\frac{1}{n}\sum_{k=1}^{n}\left(s_{ki} - \overline{\mathbf{s}_i^\top}\right)\left(s_{kj} - \overline{\mathbf{s}_j^\top}\right)}{\sqrt{\frac{1}{n}\sum_{k=1}^{n}\left(s_{ki} - \overline{\mathbf{s}_i^\top}\right)^2} \cdot \sqrt{\frac{1}{n}\sum_{k=1}^{n}\left(s_{kj} - \overline{\mathbf{s}_j^\top}\right)^2}} \begin{cases} 1, & \text{if } i = j, \\ r_{ij}, & \text{otherwise} \end{cases} \tag{7}$$

with:

S: *Gabor Spectrogram*,
r_{ij}: Correlation coefficient between columns i and j in **S**,
$\mathbf{s}_i^\top$: ith column of a *Gabor Spectrogram* **S**,
k: Running index over elements of a column vector,
s_{ki}: kth element of the ith column,
$\overline{\mathbf{s}_i^\top}$: Mean of the ith column.

Each element in R_{ij} can be seen as the normalized covariance information between combinations of frequency distributions. They represent the degree of linear relationship between the joint frequency variations in different frequency bands of all possible column combinations. The matrix R can therefore be interpreted as a map of similarities and dissimilarities along the beam axis, revealing connected regions of structural similarity in the spatial domain. The columns making up the local neighborhood inside of a cavity will therefore show to be similar when compared to other locations. The analysis of R therefore allows distinguishing between coherent regions that are sufficiently (dis-) similar to each other. This analysis allows us to identify coherent regions of related change along the beam axis.

2.3.5. Correlation method alternative
The modularity of our approach allows exchanging the method used to compute each cell in the correlation matrix. An alternative to fine-tune the approach is the *Spearman Rank Correlation*:

$$\rho_{ij} = 1 - \frac{6\sum_{k=1}^{N}\left(R\left(\mathbf{s}_{ki}^\top\right) - R\left(\mathbf{s}_{kj}^\top\right)\right)^2}{N(N^2-1)} \tag{8}$$

with:

ρ_{ij}: Spearman rank correlation coefficient, between the ith and jth columns of **S**,
S: *Gabor Spectrogram*,
N: Number of frequency bins in each column of **S**,
$\mathbf{s}_i^\top$: ith column of **S**,
$R(\mathbf{s}_{ki}^\top)$: Rank of the kth frequency bin in the ith column of **S**,
$R(\mathbf{s}_{kj}^\top)$: Rank of the kth frequency bin in the jth column of **S**.

While the more commonly used *Pearson Correlation* measures the degree of a linear relationship between the two compared *Gabor Spectrogram* columns, the *Spearman Rank Correlation* assesses how well the monotonic relationship (consistently increasing or decreasing) between two variables can be described using their ranked values, making it more robust to outliers and non-linear trends. A performance comparison between the two methods is presented in section 3 and table 1. The results show that even though the approach using Pearson correlation performs best overall, the localization approach using the Spearman correlation outperforms it when no input signal filtering is applied.

2.3.6. Depth detection of changes using the correlation matrix
The detectability of changes depends on a multitude of factors such as their size and variational structure as well as the structure of the noise originating from measurement and post-processing uncertainties. A variety of powerful methods are available from the image processing domain that are capable of improving the signal-to-noise ratio to enhance the difference information contained in the correlation matrix (see examples in figure 5). The structure of the information contained in the correlation matrix naturally lends itself to enhancements by such image filtering methods. At this stage in the analysis pipeline, they can be used to enhance the detectability of homogeneous zones of relative (dis-) similarity that relate to regions of changes. With the goal of determining a single estimate for the cavity location we analyze the gradients of the correlation matrix by first restricting the measurements to the region of

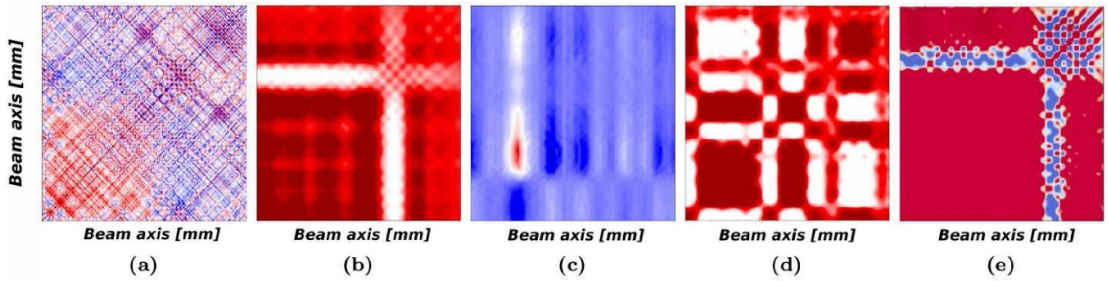

Figure 5. Showcasing the effects of applying different image filters (and combinations of filters) to the correlation matrix in (a); (b) Gaussian filter (see equation (10)) applied; (c) Bilateral median filter applied; (d) thresholding filter applied; (e) thresholding after median filter.

the head phantom in beam direction. This is a reasonable constraint, since in a clinical setting the location and dimensions of the patient will always be precisely known. We then accumulate the columns of the correlation matrix into the 1D array a by determining the sum over all of its columns.

Alternatively, at this point we have the option to choose a different accumulation operator such as the *median*, or *mode* (most common number) of the values in a column (see equation (9)). This accumulation array now represents per location bin the joint degree of (dis-) similarity compared to all other locations. In a final step we analyze the gradients of the resulting curve and determine the locations at which the largest amount of joint change occurred in the frequency domain by identifying the location of the steepest descent between the isocenter and the minimum of the curve. The resulting location we consider the detected matter transition and cavity location:

$$\begin{aligned} \text{Sum:} \quad & \text{Sum}\{\mathbf{r}_j^\top\} = \sum_{i=1}^{N} r_{ij} \\ \text{Median:} \quad & \text{Med}\{\mathbf{r}_j^\top\} = \begin{cases} r_{\left[\frac{n+1}{2}\right],j} & \text{if } n \text{ is odd} \\ \frac{1}{2}\left(r_{\left[\frac{n}{2}\right],j} + r_{\left[\frac{n+1}{2}\right],j}\right) & \text{if } n \text{ is even} \end{cases} \\ \text{Mode:} \quad & \text{Mode}\{\mathbf{r}_j^\top\} = \underset{x \in \mathbf{r}_j^\top}{\arg\min} f(x) \end{aligned} \tag{9}$$

with:

R: Correlation matrix,
$\mathbf{r}_j^\top$: jth column of correlation matrix **R**,
N: number of frequency bins in **R**,
$f(x)$: determines the number of each value x in the matrix column $\mathbf{s}_i^\top$

$$G(x,y) = \frac{1}{2\pi\sigma^2} \exp\left(-\frac{x^2+y^2}{2\sigma^2}\right) \tag{10}$$

with:

G(x, y): Gaussian weighting function at pixel location (x,y),
σ: Standard deviation of the Gaussian distribution.

2.4. Detectability quantification

One of the required building blocks of a full 3D reconstruction method is a way to determine when the data sets are too similar to perform a detection. Especially when the change covers only a small fraction of the irradiated space, the analysis needs to be able to provide some measure of detectability. Since the localization principle is based on analyzing the gradients of accumulated column values consisting of regions of varying similarity, the range of accumulated values (difference between their maximum and minimum) can be interpreted as a measure of detectability. The range differences between different measurements acquired with and without the presence of a cavity are shown in figure 6. In addition, the gradients of the accumulation curve provide us with information about the matter transition it was caused by.

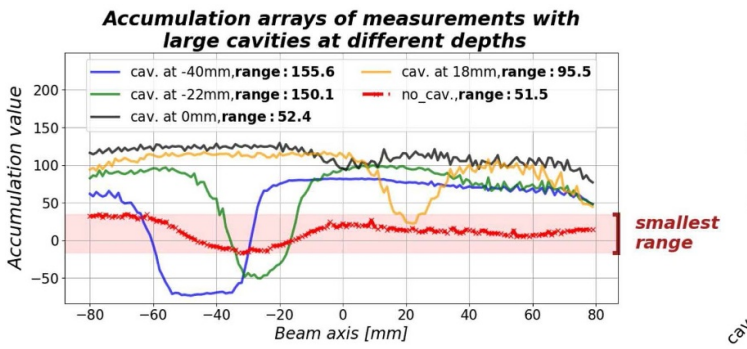

(a) Accumulation arrays of measurements with *large* cavities (left) and their respective range values (right).

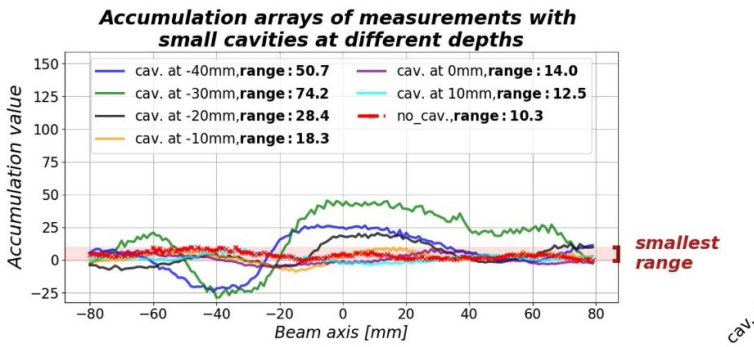

(b) Accumulation arrays of measurements with *small* cavities (left) and their respective range values (right).

Figure 6. Accumulation arrays (column sums) and their respective range values derived from correlation matrices (using Pearson correlation and no matrix filtering) of (a) large- and (b) small cavity measurements at different depths, as well as examples without cavities, showing that the range values indicate detectability and hint at the presence or absence of a cavity.

2.5. Change localization

An important motivation for exploiting more features of the secondary particle measurements was the unstable spatial correspondence between the minimum location of the difference histogram and the true cavity location. Our approach therefore focuses on increasing the robustness by identifying difference regions that can be distinguished from other regions with less dependence on the individual particle amounts at and around the cavity location. This addresses effects observed when attempting to localize a cavity at varying depths: particle amounts per location will decrease the more material had to be traversed before a cavity was encountered as it is the case with deep seated tumors (Muraro *et al* 2016, Ghesquière-Diérickx *et al* 2022). Such depth-dependent particle count depletion will increase instability when attempting to localize changes on the basis of the minimum due to higher uncertainties and a decreased signal-to-noise ratio, as can be observed in the baseline results shown in figure 9(a).

Exploiting the variational space of the measurements in the spectral domain allows exploiting common characteristics based on a broader informational foundation which stabilizes the localization performance. This can be observed in the consistency and absolute *localization loss* (we define as the absolute distance between the location estimate and the true cavity location, outside the range it covers) when comparing the performance of presented method and the baseline method in figure 9(a). Reaching these results requires a final step in our modular data analysis pipeline, which consists of solving the original depth estimation problem of localizing anatomical changes along the beam axis. The best approach for this step may depend on the filtering applied earlier in the pipeline (see figure 5 for different filtering results). Our implementation is designed to work well given our particular filtering strategy and may need to be adapted if the structure of the intermediate data products is different. This is a deliberate focus on modularity that guarantees adaptability to specific clinical circumstances. Furthermore, at this point it would be possible to apply more advanced methods capable of utilizing high-dimensional information contained in the correlation matrices to pinpoint the cavity location. The

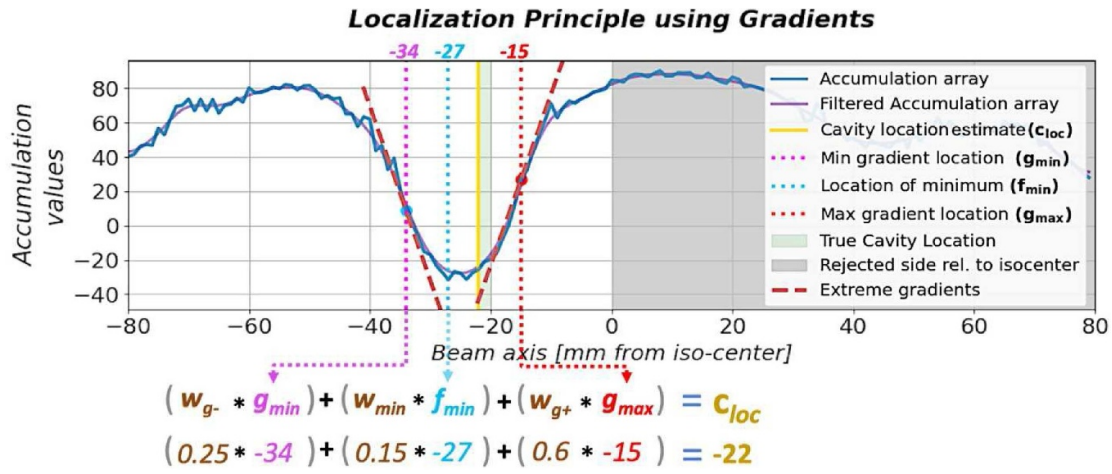

Figure 7. Visualization of the gradient based localization of a cavity at −22 mm using a weighted average of the extreme gradient locations and the minimum between them. The respective weights $w_{g-}, w_{\min}, w_{g+}$ were obtained by optimizing the localization loss over all available data sets.

regression approach used in this work is kept simple for the sake of generality and to maintain comparability with the baseline method.

Considering that only the region traversed by the treatment beam can yield secondary particles, it is reasonable to restrict the valid search space in positive beam direction (behind the target region). Given the treatment plans used during the experiments in this work, with a treated region of up to ±25 mm around the isocenter, we set it to 40 mm. The localization process starts by utilizing the array of data points computed by *summing* the columns of the correlation matrix (see accumulation in figures 8(a)–(j)(bottom)). A fixed property of the measurement setup is the centering of the tumor at the isocenter of the treatment room. All estimations will therefore be made relative to that location along the beam axis. To constraint our analysis iteratively, we determine the joint accumulation value (area under the curve) of the accumulation array before and after the isocenter separately and assume the cavity to be located on the side with the lower value. This is motivated by the observation that the regions outside of anatomical changes will be more likely to show positive correlation values among similar regions and negative correlation values for the cavity region. The subsequent analysis will determine the location of the steepest negative and positive gradients of the accumulation array restricted on that side. In order to suppress strong local gradients, we applying a Gaussian smoothing filter with a standard deviation of $\sigma = 2.0$ to the accumulation value array. We estimate the cavity location c_{loc} by determining the weighted average between the location of the smallest gradient $g_{\min}$ the largest gradient $g_{\max}$ and the location of the minimum value of the accumulation array $f_{\min}$ between the two extreme gradients (see figure 7). These three features were chosen since they are consistently available as a result of the preceding stages of the analysis pipeline and they are used to compensate for depth-dependent effects that negatively affect the correspondence between the detectable difference and the cavity location. The weights for these features were chosen such that they minimize the joint loss (the mean absolute distance between the estimate and the actual cavity location) among the available datasets. They do not need to be recomputed each time, because they reflect inherent properties of the detection setup. Within the current scope, weights derived from a small number of experiments can already yield reliable results, even though a larger database might improve them further.

3. Results

3.1. Depth detection of large and small air cavities

The results of estimating the depth location along the beam axis of analyzing measurements from irradiation experiments with large air cavities (70 mm × 70 mm on the *x*,*y*-axis of the transverse plane, with 2 mm thickness along the beam axis) inside a PMMA head phantom are shown in figure 8. The four datasets vary in the depth at which the cavity is inserted into the phantom. Irradiation was carried out with a clinically realistic treatment plan designed for a spherical tumor at the isocenter, with a diameter of 50 mm. That means that the large cavities span the entire irradiated region while the small cavities span only a fraction of that area, as depicted in figure 1(d). Since this work is focused on detecting the

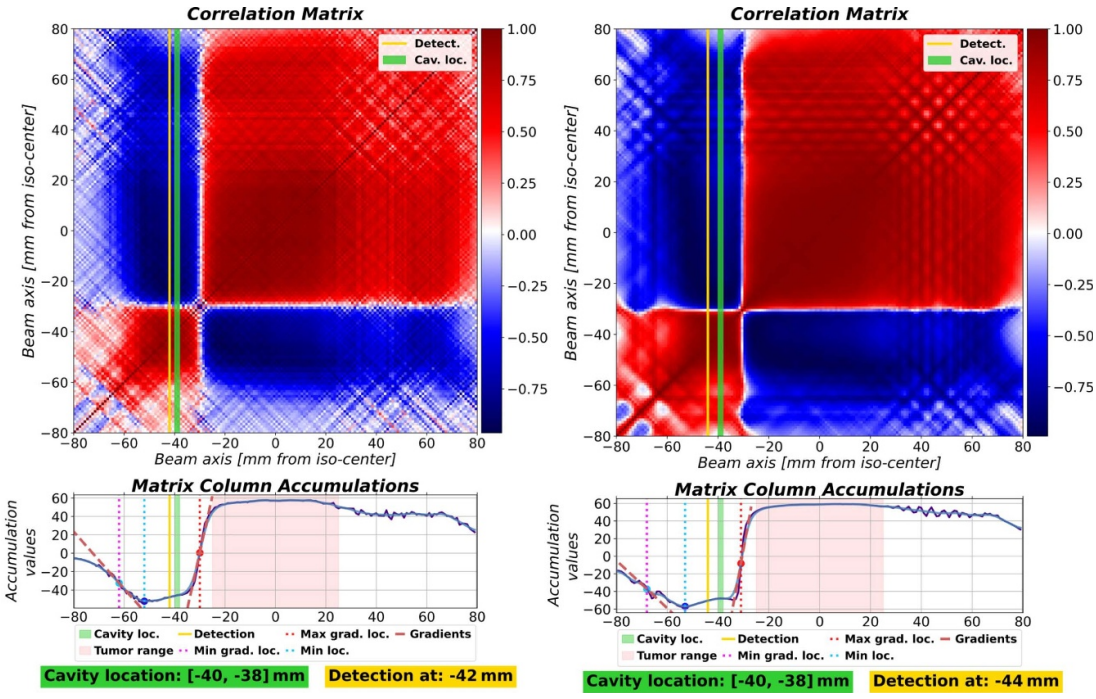

(a) Detection of a *large* cavity at $-40\,\mathrm{mm}$ along the beam axis. The resulting correlation matrix is shown unfiltered (left) and after input signal filtering (right), the matrix column accumulation function is shown at the bottom.

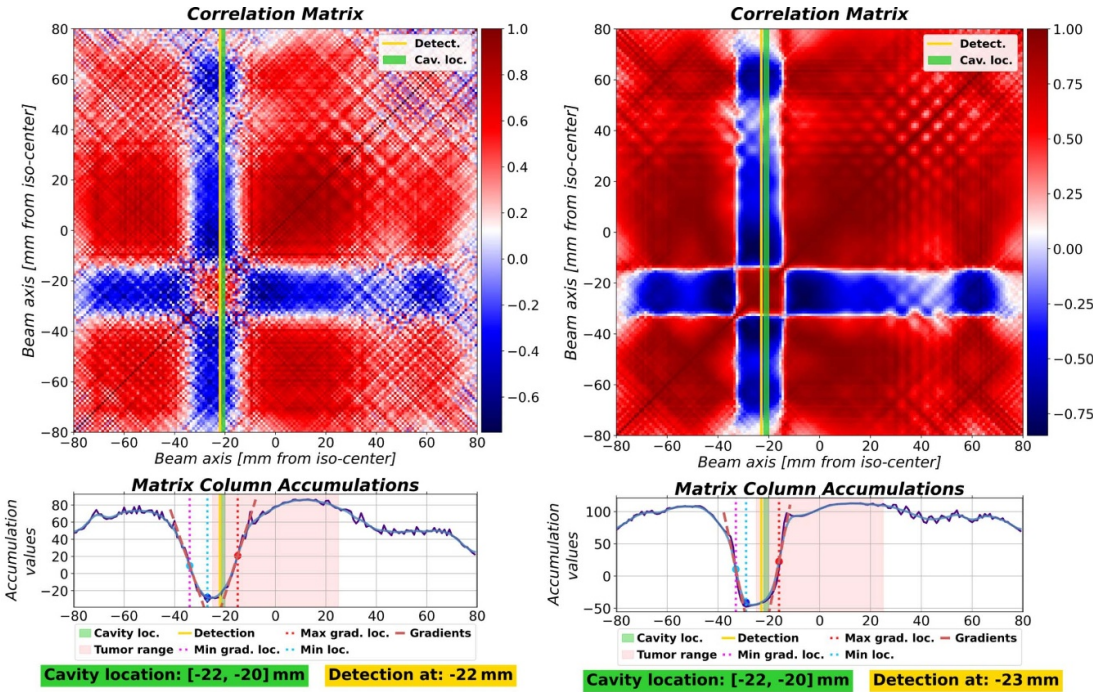

(b) Detection of a *large* cavity at $-22\,\mathrm{mm}$ along the beam axis. The resulting correlation matrix is shown unfiltered (left) and after input signal filtering (right), the matrix column accumulation is shown at the bottom.

Figure 8. Comparison of centered 41 mm × 41 mm regions, unfiltered (left) and median-filtered input signals (right) for large (a)–(d) and small (e)–(j) cavities: (Pearson-) correlation matrices (top) and the sum-accumulated columns localization (bottom).

depth of an anatomical change along the beam axis, our goal was to enable a fair and unbiased assessment of how our method would perform under varying conditions. In all cases we used the measurements of multiple repetitions of irradiating the same treatment plan, which is done to ensure statistical stability. The measurements of large and small cavities were performed under comparable experimental conditions (see section 2.1.2 and figures 1(c) and (d) for details), which resulted in different numbers of detected particles. For a fair comparison, we applied a stratified subsampling scheme that reduced

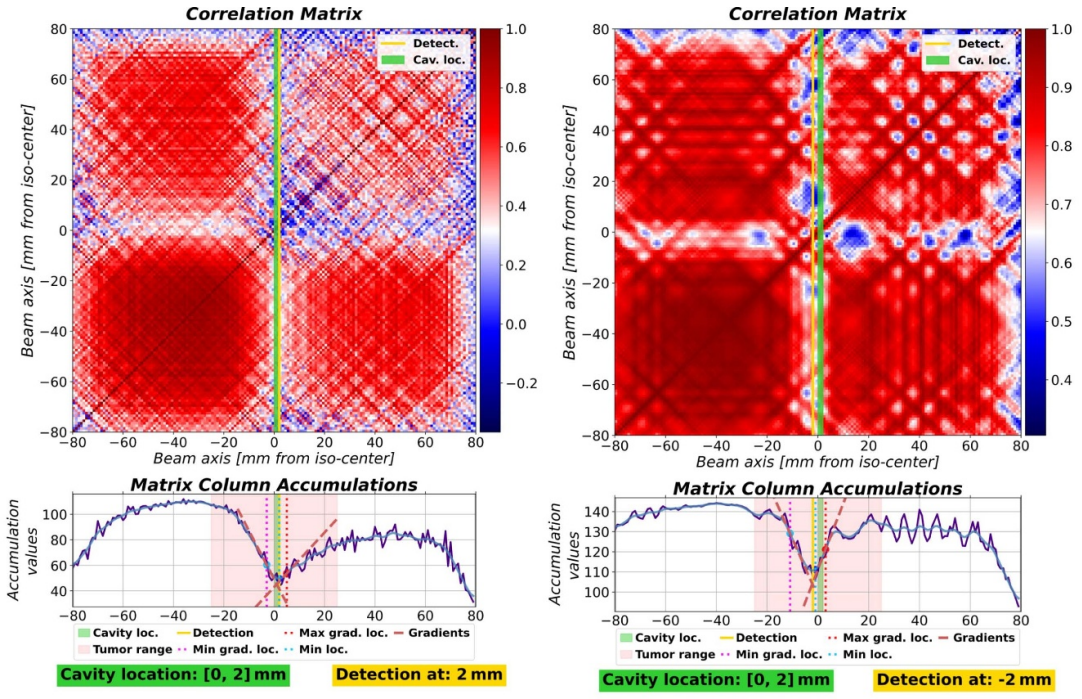

(c) Detection of a *large* cavity at 0 mm along the beam axis. The resulting correlation matrix is shown unfiltered (left) and after input signal filtering (right), the matrix column accumulation function is shown at the bottom.

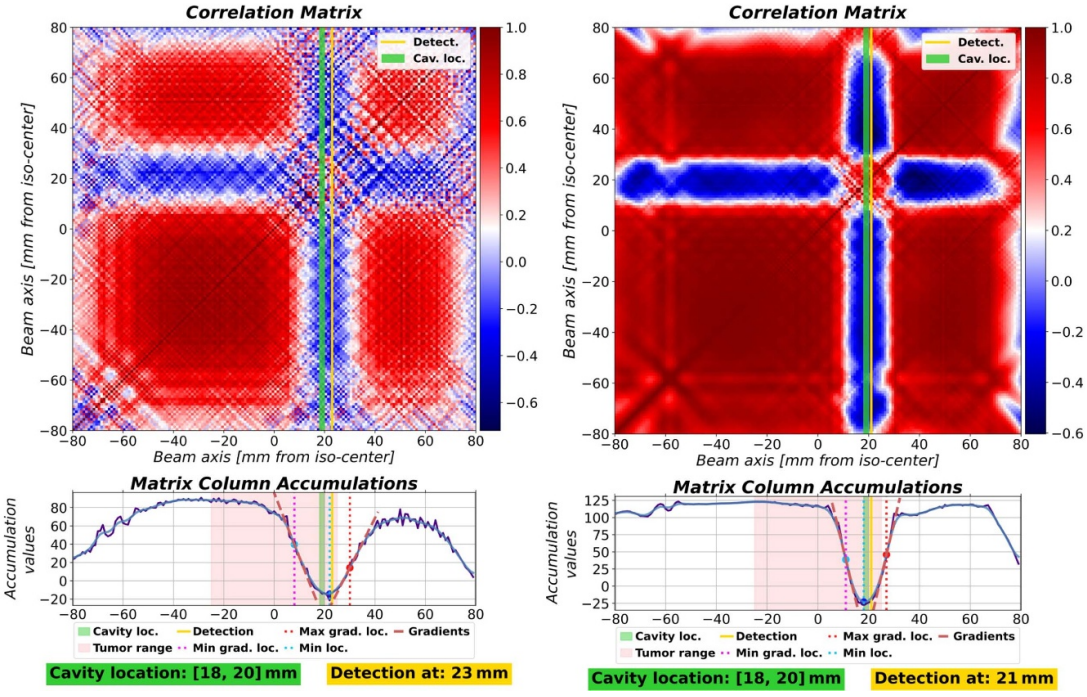

(d) Detection of a *large* cavity at 18 mm along the beam axis. The resulting correlation matrix is shown unfiltered (left) and after input signal filtering (right), the matrix column accumulation function is shown at the bottom.

Figure 8. (Continued.)

the number of measurements in large cavity datasets while preserving data density, resulting in similar amounts of particle origins across all data sets. The subsampling method employed ensured that the underlying particle distributions were not affected by removing a fraction of the data. Furthermore, to ensure comparability, we performed our analysis on the same window located at the center of the transverse plane with a size of 41 mm × 41 mm which preserves the presence of a dominant amount of area without a cavity in the window ($\approx 77\%$). This allows investigating the effect of the additional noise contribution this results in.

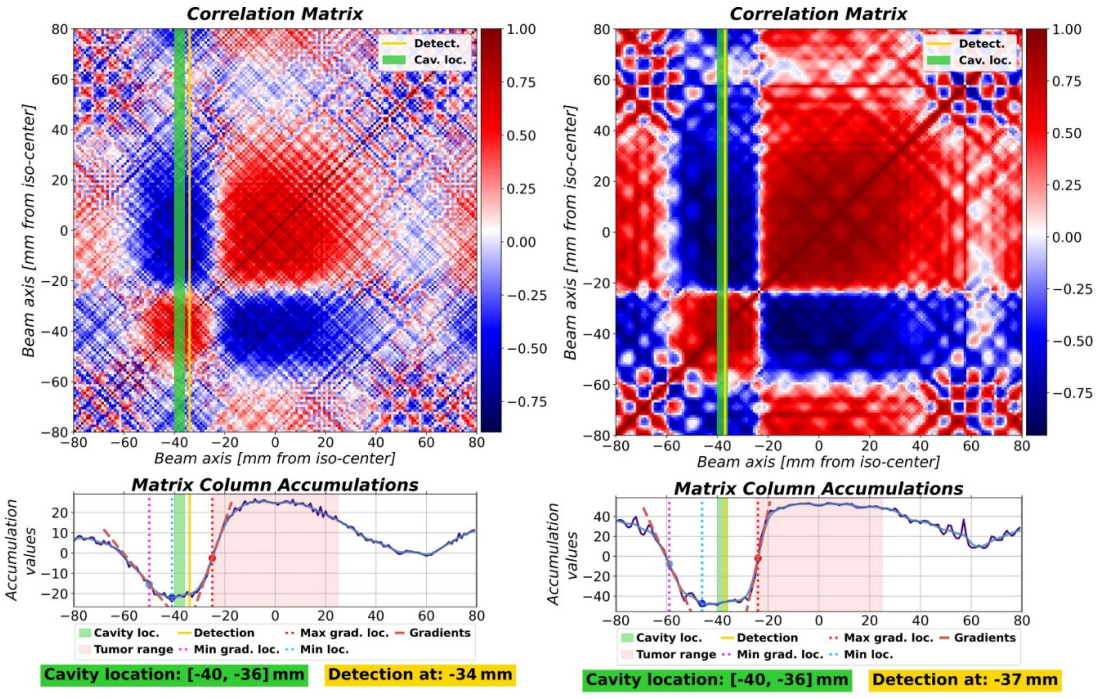

(e) Detection of a *small* cavity at $-40\,\mathrm{mm}$ along the beam axis. The resulting correlation matrix is shown unfiltered (left) and after input signal filtering (right), the matrix column accumulation function is shown at the bottom.

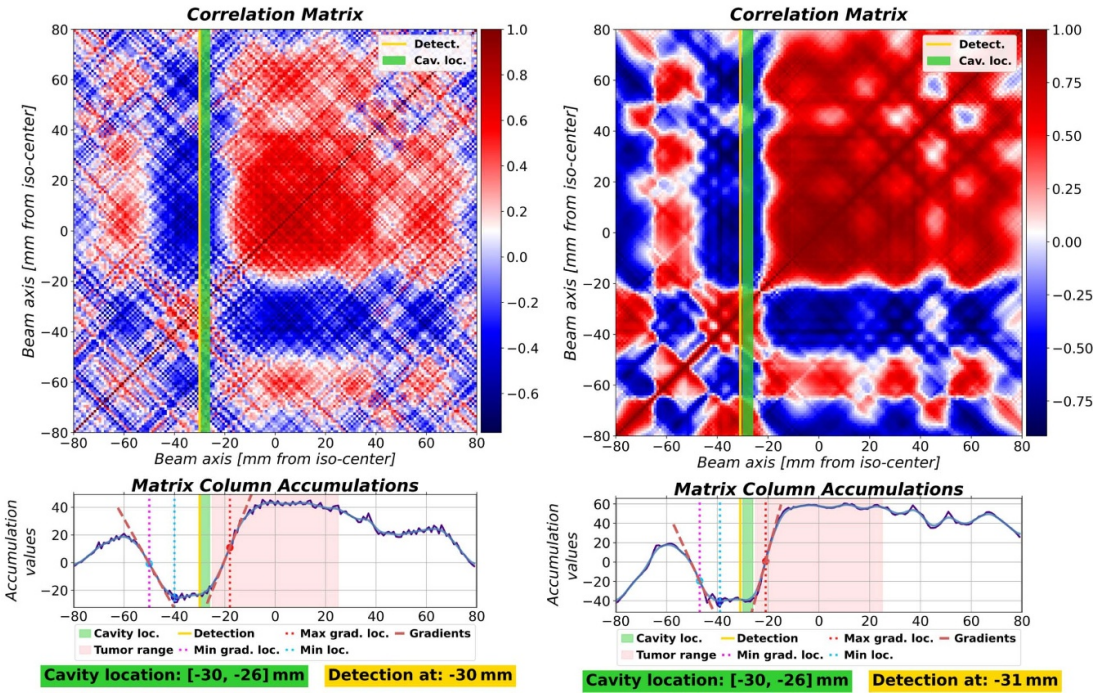

(f) Detection of a *small* cavity at $-30\,\mathrm{mm}$ along the beam axis. The resulting correlation matrix is shown unfiltered (left) and after input signal filtering (right), the matrix column accumulation function is shown at the bottom.

Figure 8. (Continued.)

All results were repeated applying the same edge-preserving median filter (see equation (9)) to the input signal (the difference histogram) to reduce noise in the signal while preserving as much of its relevant variations and their frequency contributions. Even though our approach allows filtering at various stages of the processing pipeline, for comparability, we restricted filtering to the input signal (the difference histogram) which is also directly used by the baseline detection method. The baseline detection method estimates the depth along the beam axis in the spatial domain by determining the location of the minimum of the difference histogram as proposed in Ghesquière-Diérickx *et al* (2022).

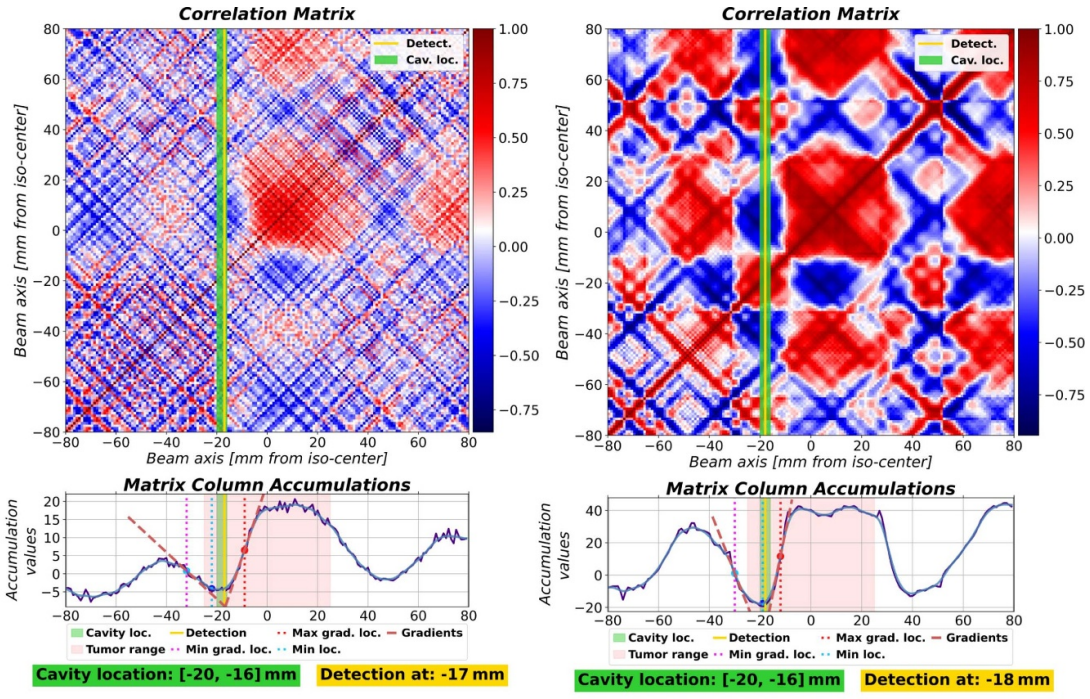

(g) Detection of a *small* cavity at $-20\,\mathrm{mm}$ along the beam axis. The resulting correlation matrix is shown unfiltered (left) and after input signal filtering (right), the matrix column accumulation function is shown at the bottom.

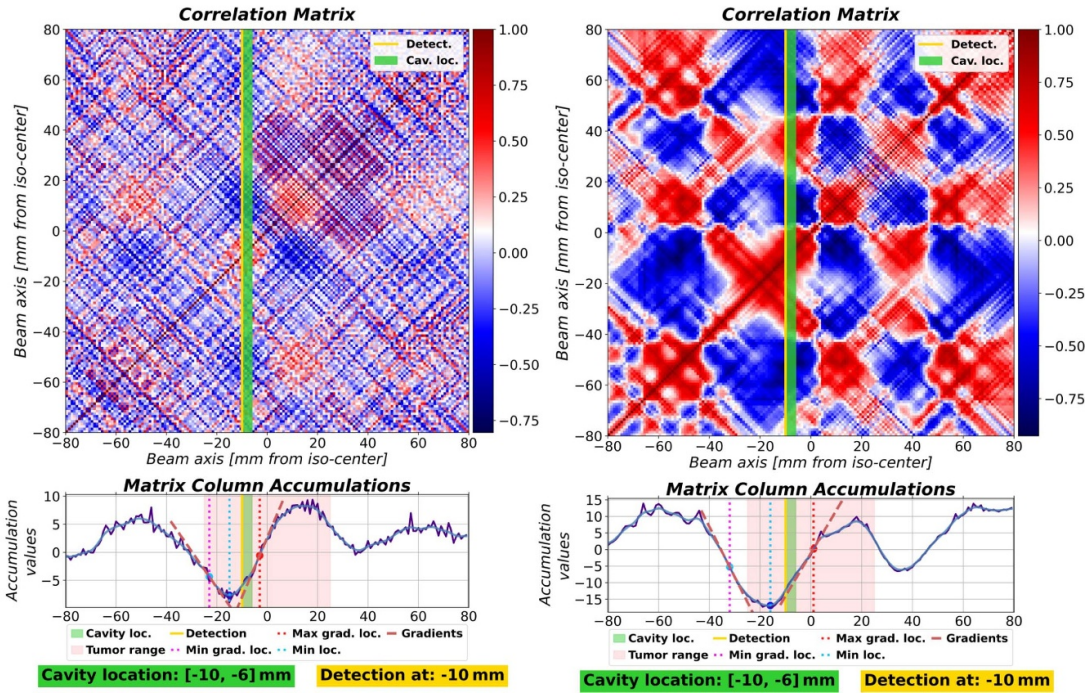

(h) Detection of a *small* cavity at $-10\,\mathrm{mm}$ along the beam axis. The resulting correlation matrix is shown unfiltered (left) and after input signal filtering (right), the matrix column accumulation function is shown at the bottom.

Figure 8. (Continued.)

Table 1 and figure 9(b) show that there is no improvement in the mean absolute localization loss (see its definition in section 2.5) for the baseline method while using the same input signal filtering the presented method improves in performance (see figures 9 and 8 (left vs. right)). To be able to validate the presented method we utilize the gradients of the accumulated matrix columns to localize the cavity along the beam axis as described in section 2.5.

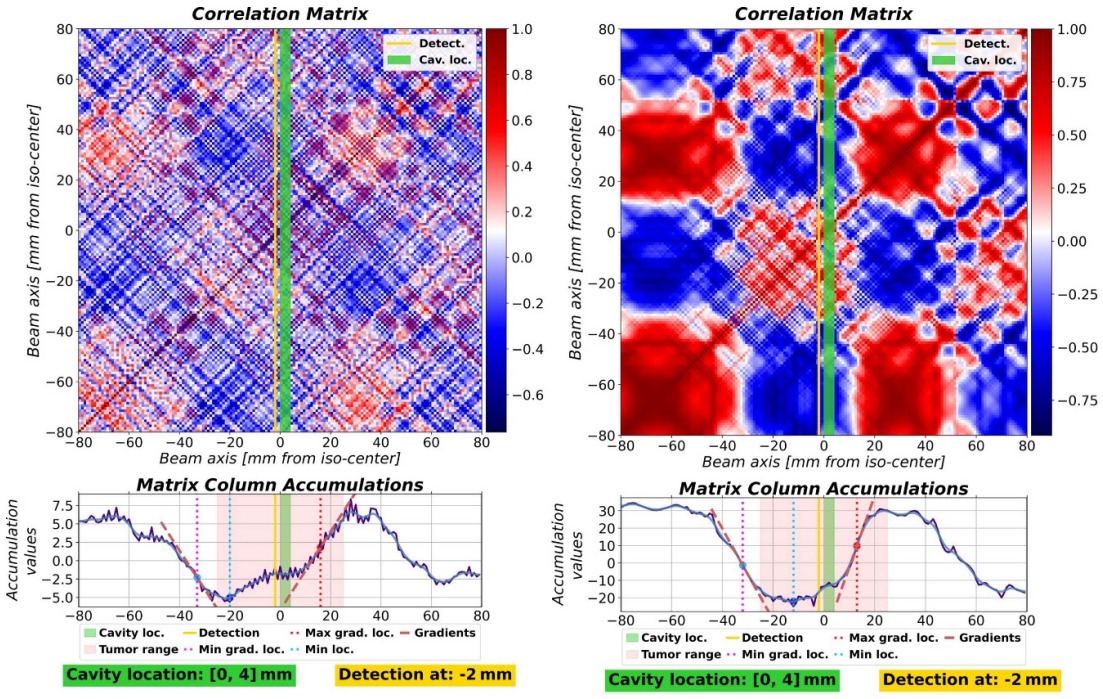

(i) Detection of a *small* cavity at 0 mm along the beam axis. The resulting correlation matrix is shown unfiltered (left) and after input signal filtering (right), the matrix column accumulation function is shown at the bottom.

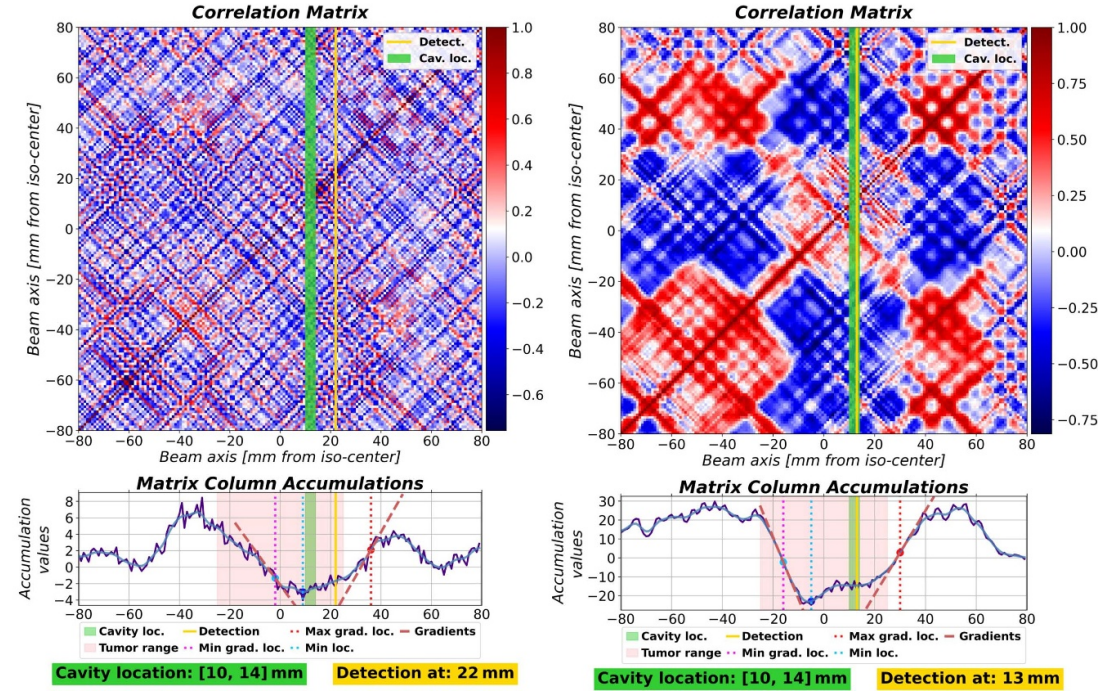

(j) Detection of a *small* cavity at +10 mm along the beam axis. The resulting correlation matrix is shown unfiltered (left) and after input signal filtering (right), the matrix column accumulation function is shown at the bottom.

Figure 8. (Continued.)

3.2. Alternative correlation method results

As a demonstration of the modularity and flexibility of our approach, we report the results of an analysis experiment using an alternative correlation method. We exchanged the *Pearson Correlation Coefficient* computation with the *Spearman rank coefficients*, as described in section 2.3.5. In table 1 under the handle *Pres. Method (‡)* its performance is listed because of its good performance in the unfiltered setting. It shows the potential of the presented approach to be adapted to the challenges of varying measurement conditions.

Table 1. Performance comparison between the baseline method (filtered and unfiltered for fair comparison) and the presented approach using both correlation method variants (Pearson (†) and Spearman (‡)), each with and without input median filtering. The performance comparisons are based on the localization loss defined in section 2.5.

Method	min loss (mm)	max loss (mm)	loss SD[a] (mm)	mean abs. loss (mm)
Baseline (unfiltered)	0.0	89.0	32.64	39.4
Baseline (median filtered)	0.0	75.0	30.59	30.3
Pres. Method (unfiltered)†	0.0	8.0	2.37	1.7
Pres. Method (median filtered)†	0.0	4.0	**1.22**	**1.1**
Pres. Method (unfiltered)‡	0.0	6.0	2.00	1.3
Pres. Method (median filtered)‡	0.0	4.0	1.40	1.2

[a] SD = standard deviation.

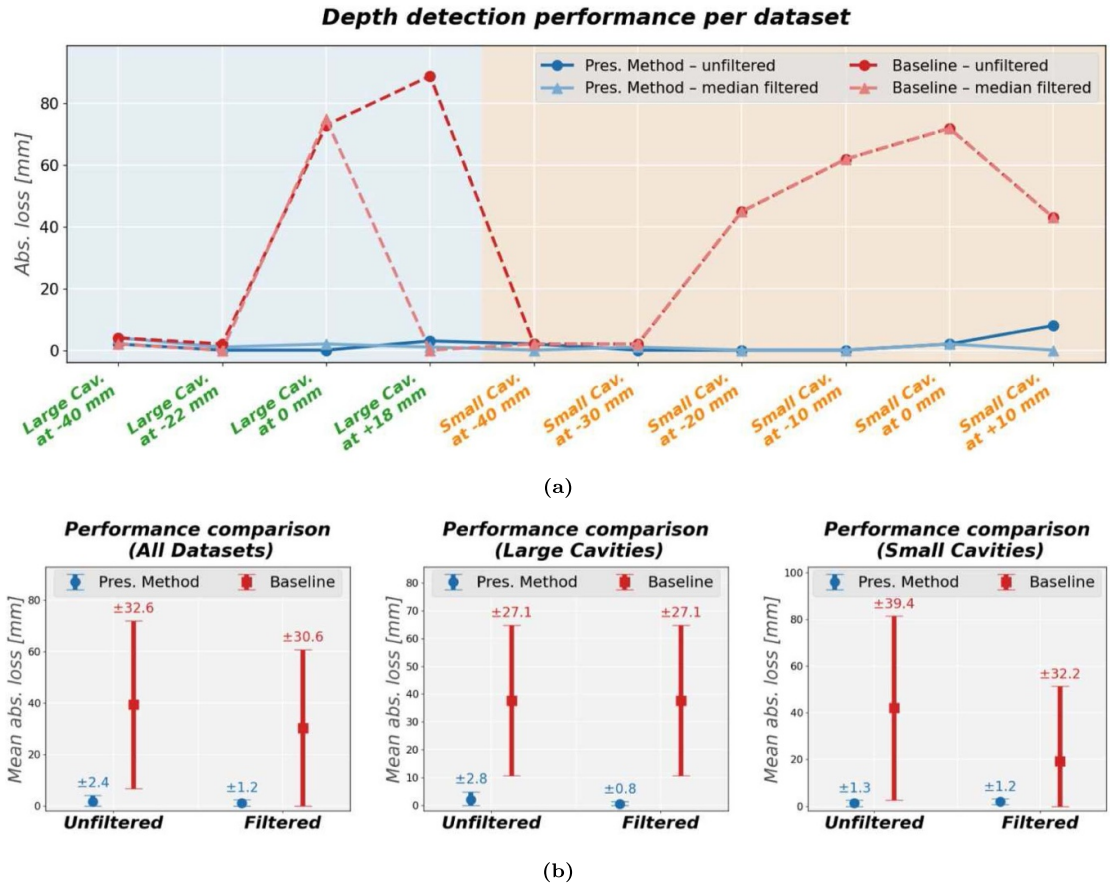

Figure 9. (a) Comparing the individual depth detection performance between our method and the baseline method for each dataset individually. (b) Comparing the mean localization loss and standard deviation of our method and the baseline method both filtered and unfiltered respectively (using Pearson Correlation).

4. Discussion

Analyzing data originating from secondary particle measurements poses challenges originating from both the measurement process as well as the stochastic nature of carbon-ion interaction processes with matter. Despite these challenging signal-to-noise conditions under which we seek to detect and localize anatomical changes between sets of measurements our presented method is capable of providing precise location estimation.

In clinical practice, personalized distributions of the administered dose as well as the individual structure of the treated regions will result in natural variations in the number of available particle origins per location. Therefore, a robustness to varying amounts of measured particles is a highly desirable property when aiming for the ability to generalize well. We demonstrate that the use of the spectral domain improves detection and localization robustness, as it relies on analyzing density variations of measurement sets and does not require locally stable particle counts across different measurements. In addition, gaining access to the spectral domain allows us to mitigate effects inherent to the irradiation

and measurement procedures. An example is the pencil beam scanning process depicted in figure 2(b), which is comprised of discrete treatment beam steps, imprinted in the particle origin distribution. Our method allows us to mitigate these types of decremental effects present in all data sets, due to focusing on the variations of the spectral components along the beam axis. Since the density variations of particle subsets directly relate to the interaction principles of ion-beams with matter, our approach and its intermediate analysis steps allow it to be interpreted based on basic physical principles common to the particle therapy domain. Transforming the spectral data back to a two-dimensional matrix with discernible spatial regions, we enable the use of well-established methods from the signal- and image processing domains, capable of enhancing structural signals in the presence of noise. This way we are able to increase the spatial resolution of our approach since the expected anatomical differences between consecutive treatment fractions are very small in clinical reality. Our method also provides a means of determining the uncertainty of a depth estimate by exploiting variations in inter-locational similarities and dissimilarities. Comparing our results with those of the baseline method, which detects changes based solely on the maximal difference location between two histograms, we demonstrate much higher localization precision and more consistent results across varying datasets. This higher accuracy is maintained even under more challenging experimental conditions, with smaller cavities that cover only a fraction of the irradiated field and more closely approximate clinically realistic volumes.

So far, our framework has been validated on only a limited range of experimental data, which will need to be extended as development progresses toward clinical applicability. Furthermore, only for the most dominant anatomical change, a depth location estimate is provided. To address these limitations, we intend to leverage the core design principle of our framework which was to provide reusable, flexible building blocks to facilitate the design of complex analytical workflows. In fact, we can apply it in this case in the same way we envisioned it to be used to achieve a full 3D reconstruction, by reusing the presented depth detection method and apply it to subregions of the measurement set at varying locations. In combination with our detectability quantification method, for which we are developing a supporting spatial-domain extension, we can exclude regions without detectable anatomical changes and precisely estimate those showing clear evidence of them. This allows us to iteratively build a 3D reconstruction while clearly isolating and separating credible anatomical changes that are simultaneously present at different depths for precise individual localization estimates. Additionally, we intend to provide physicians with detectability quantification values visually mapped onto the reconstructions, allowing them to adjust their overall confidence in them. These approaches, however, will be extensions for future work that can be constructed from the basic components provided in this manuscript.

5. Conclusion

The data analysis procedure presented in this manuscript provides an approach for detecting and localizing the depth of changes between carbon-ion radiation treatment fractions along the beam axis. As part of a larger carbon-ion radiation therapy monitoring effort the presented procedure is designed to provide flexible building blocks for a full 3D reconstruction approach for anatomical changes using only secondary charged particle measurements. Approaching the subject in an incremental manner we have shown that the presented method is capable of localizing changes along the beam axis with a mean accuracy below 2 mm over a set of 10 different experimental measurements with cavities of varying sizes at varying depth locations. The presented method is flexible and robust and consists of components that allow fine-tuning to meet the challenges of the more complex clinical measurements.

Data availability statement

The data cannot be made publicly available upon publication because they are owned by a third party and the terms of use prevent public distribution. The data that support the findings of this study are available upon reasonable request from the authors.

Acknowledgment

This work has been carried out as part of a HIDSS4Health funded project. The authors thank the Heidelberg Ion-Beam Therapy Center (HIT) for the provided beam time.

ORCID iDs

Patrice Schlegel 0009-0003-6137-0152
Rebekka Kirchgaessner 0009-0004-1156-6226
Pamela Ochoa Parra 0009-0002-7373-7524
Laurent Kelleter 0000-0003-4346-9741
Michael Gertz 0000-0003-4530-6110
Ralf Mikut 0000-0001-9100-5496
Oliver Jäkel 0000-0002-6056-9747
Maria Martišíková 0000-0001-6104-0397

References

Amaldi U and Kraft G 2005 Radiotherapy with beams of carbon ions *Rep. Prog. Phys.* **68** 1861
Attinger E O, Anné A and McDonald D A 1966 Use of Fourier series for the analysis of biological systems *Biophys. J.* **6** 291–304
Blackman R B and Tukey J W 1958 The measurement of power spectra from the point of view of communications engineering - part 1 *Bell Syst. Tech. J.* **37** 185–282
Bracewell R 2012 *Fourier Analysis and Imaging* (Springer)
Durante M and Debus J 2018 Heavy charged particles: does improved precision and higher biological effectiveness translate to better outcome in patients? *Sem. Radiat. Oncol.* **28** 160–7
Félix-Bautista R *et al* 2021 Quality assurance method for monitoring of lateral pencil beam positions in scanned carbon-ion radiotherapy using tracking of secondary ions *Med. Phys.* **48** 4411–24
Gaa T, Reinhart M, Hartmann B, Jakubek J, Soukup P, Jäkel O and Martišíková M 2017 Visualization of air and metal inhomogeneities in phantoms irradiated by carbon ion beams using prompt secondary ions *Phys. Medica* **38** 140–7
Gabor D 1946 Theory of communication. Part 1: the analysis of information *J. Inst. Electr. Eng. III* **93** 420–41
Ghesquière-Diérickx L *et al* 2022 Detecting perturbations of a radiation field inside a head-sized phantom exposed to therapeutic carbon-ion beams through charged-fragment tracking *Med. Phys.* **49** 1776–92
Ghesquière-Diérickx L, Schlechter A, Félix-Bautista R, Gehrke T, Echner G, Kelleter L and Martišíková M 2021 Investigation of suitable detection angles for carbon-ion radiotherapy monitoring in depth by means of secondary-ion tracking *Front. Oncol.* **11** 221
Gunzert-Marx K, Iwase H, Schardt D and Simon R S 2008 Secondary beam fragments produced by 200 MeV/u ^{12}C ions in water and their dose contributions in carbon-ion radiotherapy *New J. Phys.* **10** 075003
Gwosch K, Hartmann B, Jakubek J, Granja C, Soukup P, Jäkel O and Martišíková M 2013 Non-invasive monitoring of therapeutic carbon ion beams in a homogeneous phantom by tracking of secondary ions *Phys. Med. Biol.* **58** 3755
Henriquet P *et al* 2012 Interaction vertex imaging (IVI) for carbon ion therapy monitoring: a feasibility study *Phys. Med. Biol.* **57** 4655–69
Kelleter L *et al* 2024a An in-vivo treatment monitoring system for ion-beam radiotherapy based on 28 Timepix3 detectors *Sci. Rep.* **14** 15452
Kelleter L *et al* 2024b Characterisation of a customised 4-chip Timepix3 module for charged-particle tracking *Radiat. Meas.* **173** 107086
Malouff T D, Peterson J L, Mahajan A and Trifiletti D M 2019 Carbon ion radiotherapy in the treatment of gliomas: a review *J. Neuro-Oncol.* **145** 191–9
Mizoe J *et al* 2012 Results of carbon ion radiotherapy for head and neck cancer *Radiother. Oncol.* **103** 32–37
Mohamad O, Yamada S and Durante M 2018 Clinical indications for carbon ion radiotherapy *Clin. Oncol.* **30** 317–29
Muraro S *et al* 2016 Monitoring of hadrontherapy treatments by means of charged particle detection *Front. Oncol.* **6** 177
Musha A *et al* 2022 Carbon-ion radiotherapy for inoperable head and neck bone and soft-tissue sarcoma: prospective observational study *Anticancer Res.* **42** 1439–46
Nastar C and Ayache N 1996 Frequency-based nonrigid motion analysis: application to four dimensional medical images *IEEE Trans. Pattern Anal. Mach. Intell.* **18** 1067–79
Northcliffe L and Schilling R 1970 Range and stopping-power tables for heavy ions *At. Data Nucl. Data tables* **7** 233–463
Parodi K and Polf J C 2018 *In vivo* range verification in particle therapy *Med. Phys.* **45** e1036–50
Reinhart A M, Spindeldreier C K, Jakubek J and Martišíková M 2017 Three dimensional reconstruction of therapeutic carbon ion beams in phantoms using single secondary ion tracks *Phys. Med. Biol.* **62** 4884–96
Schober P, Boer C and Schwarte L 2018 Correlation coefficients: appropriate use and interpretation *Anesthesia Anal.* **126** 1
Schweins L *et al* 2025 Detection of an internal density change in an anthropomorphic head phantom via tracking of charged nuclear fragments in carbon-ion radiotherapy *Med. Phys.* **52** 2399–411
Shannon C E 1949 Communication in the presence of noise *Proc. IRE* **37** 10–21
Tinganelli W and Durante M 2020 Carbon ion radiobiology *Cancers* **12** 3022
Tureček D, Jakubek J and Soukup P 2016 USB 3.0 readout and time-walk correction method for Timepix3 detector *J. Instrum.* **11** C12065